nature physics

Article

https://doi.org/10.1038/s41567-023-02150-z

Fluid superscreening and polarization following in confined ferroelectric nematics

Received: 29 September 2022

Accepted: 27 June 2023

Published online: 27 July 2023

Check for updates

Federico Caimi[1], Giovanni Nava[1], Susanna Fuschetto[1], Liana Lucchetti[2], Petra Paiè[3,4], Roberto Osellame[4], Xi Chen[5], Noel A. Clark[5], Matthew A. Glaser[5] ✉ & Tommaso Bellini[1] ✉

The recently discovered ferroelectric nematic (N_F) liquid-crystal phase exhibits a spontaneous polarization field that is both orientationally fluid like a liquid crystal and large in magnitude like a solid ferroelectric. This combination imparts this phase with a unique electrostatic phenomenology and response to applied fields. Here we probe this phase by applying a small electric field to ferroelectric nematics confined in microchannels that connect electrodes through straight and curved paths and find that the N_F phase smoothly orders with its polarization following the channels despite their winding paths. This implies a corresponding behaviour of the electric field. On inversion of the electric field, the polar order undergoes a multistage switching process dominated by electrostatic interactions. We also find multistage polarization switching dynamics in the numerical simulations of a quasi-two-dimensional continuum model of channel-confined N_F liquid crystals, enabling the exploration of their internal structural and electrical self-organization. This indicates that polarization alignment and electric-field guiding are direct consequences of fluid superscreening—the prompt elimination of electric-field components normal to the channel walls by polarization reorientation. This response mimics the behaviour expected for ultrahigh-permittivity dielectrics, but with patterns of charge accumulation and local ordering unique to fluid ferroelectrics.

The discovery of molecules capable of ordering into a ferroelectric nematic (N_F) liquid crystal (LC), a state predicted a century ago[1–3] but only recently observed[4–7], has attracted immediate interest because of the novel properties of this new fluid state, involving its electric behaviour, its elasticity and its nonlinear susceptibilities[8–14]. Conventional nematic LCs are non-polar anisotropic fluids, in which molecules partially align along a common axis, the so-called nematic director **n**. In the N_F phase, a bulk electric polarization density **P** develops parallel to **n** through a weak first-order phase transition. Molecules found to give rise to N_F ordering have large permanent electric dipoles (>10 D) and a high degree of polar orientational order, resulting in a large ferroelectric polarization, up to $P_0 = |\mathbf{P}| \approx 6\ \mu C\ cm^{-2}$ (refs. 6,15,16).

The presence of a bulk polarization field that is readily reoriented makes the electric-field response of N_F markedly different from the dielectric response of conventional nematics, in ways that have yet to be fully explored. Because of the dielectric anisotropy of conventional nematics, the electric field (**E**) has a tensorial coupling to **n**, producing torques on the director proportional to E^2 and of a magnitude

[1]Department of Medical Biotechnology and Translational Medicine, University of Milano, Milano, Italy. [2]SIMAU Department, Università Politecnica delle Marche, Ancona, Italy. [3]Dipartimento di Fisica, Politecnico di Milano, Milano, Italy. [4]Istituto di Fotonica e Nanotecnologie, Consiglio Nazionale delle Ricerche (IFN-CNR), Milano, Italy. [5]Department of Physics and Soft Materials Research Center, University of Colorado, Boulder, CO, USA.
✉e-mail: matthew.glaser@colorado.edu; tommaso.bellini@unimi.it

https://doi.org/10.1038/s41567-023-02150-z

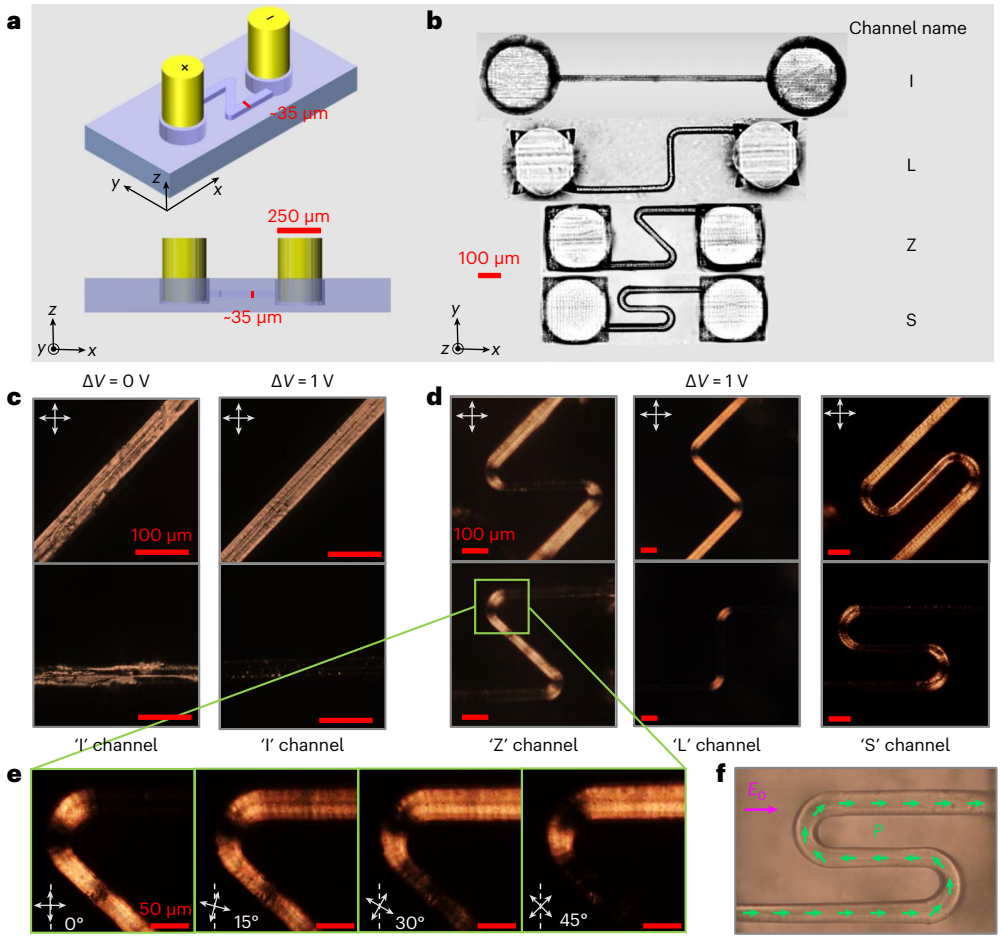

Fig. 1 | Ferroelectric nematic ordering in microchannels. a, Drawing of the buried microchannels. The yellow cylinders represent the gold wire electrodes. **b**, Pictures of the four channels considered in this work, designed so that the central part forms an angle of 0°, 90°, 135° and 180° with respect to the *x* axis. **c**, PTOM pictures between crossed polarizers in the absence (left) and presence (right) of an electric field of the I-shaped channel filled with RM734 in the N_F phase at $T = 130$ °C. The fully dark appearance of the channel in the bottom-right picture indicates that in the presence of a field, the orientation of the nematic director is along the channel. **d**, PTOM pictures between the crossed polarizers of the Z-, L- and S-shaped channels, filled with RM734 in the N_F phase at $T = 130$ °C and oriented so that the lateral portions are at 45° (top) or along (bottom) the analyser, whereas $\Delta V = 1$ V is applied to the electrodes. **e**, Enlargement of a curved portion of the Z-shaped channel at various orientations with respect to the polarizer, as indicated. **f**, Sketch of the continuity of the direction of polarization **P** (green arrows) within the S-shaped channel, indicating that in its central section, the polarization is pointing in the direction opposite to the nominal applied electric field E_0.

comparable with the orientational elasticity. In the N_F phase, the presence of a bulk polarization gives rise to a dipolar coupling to **E** and to the self-interaction of polarization space charges that can accumulate on surfaces ($\sigma_P = \mathbf{P} \cdot \mathbf{u}$, where **u** is the unit vector normal to a limiting surface of N_F) and in the bulk ($\rho_P = -\nabla \cdot \mathbf{P}$), which produce electric torques orders of magnitude larger than those derived from elastic deformations.

All these factors combine to create a fundamentally new kind of fluid, markedly different from conventional nematic LCs and from solid ferroelectric materials, whose polarization—intrinsically constrained by the symmetry of the crystal unit cell—is typically limited to a set of easy-axis orientations. In this work, we explore the interplay of external fields, geometry and electrostatic self-interaction in N_F fluids confined within straight and bent microchannels.

Description of the experiment

We have produced, via femtosecond laser micromachining assisted by chemical etching[17,18], microchannels buried in monolithic fused silica that connect gold wire electrodes. The channels (Fig. 1a,b) are all of length $\ell \approx 1$ mm and have a rounded square cross section of width $w \approx 35$ µm. Four different shapes were produced: straight along the *x*-axis direction connecting the electrodes (I-shaped channel), with the central part forming an angle with respect to the *x* axis of 90° (L-shaped channel), 135° (Z-shaped channel) and 180° (S-shaped channel) (Fig. 1b). The channels were filled with RM734, an LC material that exhibits nematic (N) and ferroelectric nematic (N_F) phases[4,6], with the N–N_F transition temperature $T_{N-N_F} \approx 133$ °C. Before filling, the glass channel surfaces were silanized with hexadecyltrimethoxysilane to favour the planar orientation of RM734 (ref. 19). Supplementary Section 1 provides a detailed description of the fabrication process.

Response to static fields

In the absence of an applied voltage difference ΔV between the electrodes, the nematic director exhibits partial ordering along the channel in both N and N_F phases. By applying a voltage ΔV, which gives rise to a 'nominal' electric field $E_0 \equiv \Delta V/\ell$, the N_F ordering becomes virtually perfect in all the four channels when $E_0 > 0.25$ V mm^{-1} (Fig. 1c,d), whereas no substantial effect is visible in the N phase for fields up to $E_0 \approx 50$ V mm^{-1} (Supplementary Fig. 1). We closely inspected the field-induced N_F alignment by polarized transmission optical microscopy (PTOM) and by second-harmonic generation microscopy (Supplementary Fig. 2) and found no sign of either defect lines or defect

https://doi.org/10.1038/s41567-023-02150-z

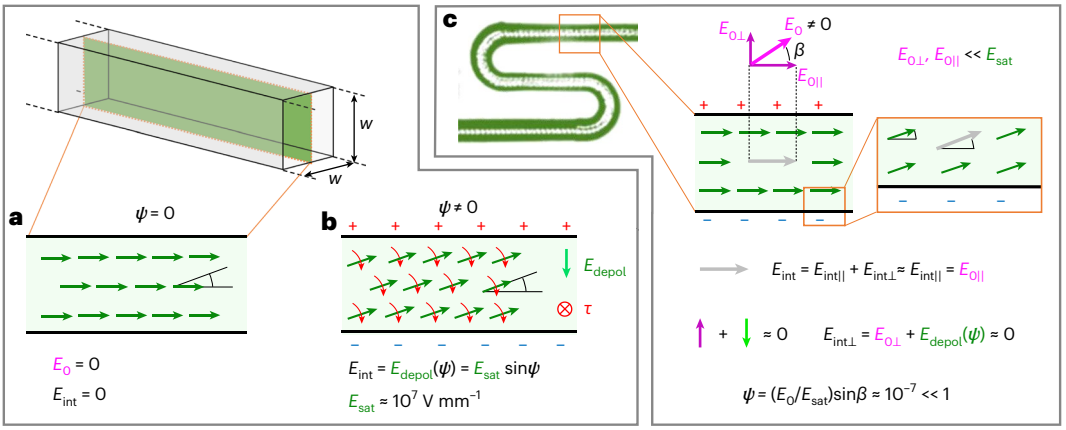

Fig. 2 | Schematic of the fluid superscreening in a channel. a, Longitudinal mid-section of an ideal smooth channel of infinite length and square section. In the absence of external fields ($E_0 = 0$), the reorientable polarization field **P** (green arrows) aligns along the channel axis ($\psi = 0$), a condition by which the electric field inside the channel is $E_{int} = 0$. **b**, When $\psi \neq 0$, polarization charges accumulate at the channel edges, giving rise to a depolarization field E_{depol} and a torque $\tau = P_0 E_{depol} \cos\psi$ acting to re-establish the $\psi = 0$ condition. **c**, In the experiments, applied electric fields $\mathbf{E}_0$ are not generally oriented along the channel direction, with components $E_{0\parallel}$ and $E_{0\perp}$ along and perpendicular to the channel axis, respectively. Although $E_{0\parallel}$ is continuous across the channel walls, $E_{0\perp}$ is cancelled by superscreening. Since the applied fields are much smaller than E_{sat}, the tilt angle ψ necessary for such cancellation is too small to be detectable (in the zoomed-in view, ψ is enhanced to enable representation).

walls even in the curved sections of the channels that bend contrary to the naive electrode-to-electrode direction expected for E_0 in uniform dielectrics (Fig. 1e). This finding indicates that under these conditions, both nematic director **n** and polarization **P** are always nearly parallel to the solid surface and continuously follow the channel ('polarization following') (Fig. 1f). The continuity of N_F polarization along the channels also implies a similar continuity of the electric field, which, thus, follows the channels rather than being directed along the paths connecting the electrodes as in homogeneous dielectric media. This behaviour is not dissimilar to what happens in a bent conductive wire between electrodes, where the surface accumulation of free charges steers the field along the wire, independent of its path. In N_F materials, an analogous effect arises from the redistribution of bound charges.

Ferroelectric superscreening

We understand the continuity of polarization and electric field along the channels as the effect of the orientational freedom of **P** in the N_F phase, which is, in turn, a consequence of the symmetry, energy degeneracy and fluidity of the LC. Reorientations of **P** enable an immediate deposition of bound charges that readily cancels the normal component of **E** within the channel, which, thus, becomes parallel to the channel axis.

We sketch this phenomenon in Fig. 2, where we consider an N_F LC confined to a channel and assume that both N_F material and confining substrate have an isotropic relative permittivity of unity ($\epsilon_r = 1$), a condition that enables singling out the effects of the spontaneous fluid **P**, whose local amplitude P_0 is uniform, being determined only by T.

In an idealized channel of infinite length and in the absence of an external electric field, the polarization is parallel to the channel ($\psi = 0$) and $\mathbf{E} = 0$ (Fig. 2a). This is because $\psi \neq 0$ would result in the deposition of surface polarization charge $\sigma_P = \mathbf{P} \cdot \mathbf{u} = P_0 \sin\psi$ on the channel surfaces (Fig. 2b), generating a depolarization field of magnitude $E_{depol} = P_0 \sin\psi / \varepsilon_0$ within the channel. The depolarization field provides a restoring torque density that opposes the reorientation, a sort of electrostatic orientational spring that tends to force ψ back to zero. This electrostatic spring is exceptionally stiff, as evident in estimating the saturation depolarization field $E_{sat} = P_0/\epsilon_0$ generated in the channel when $\psi = 90°$. For $P_0 \approx 6 \times 10^{-2}$ C m^{-2}, this condition would yield a gigantic $E_{sat} \approx 10^7$ V mm^{-1}, demonstrating that **P** perpendicular to the channel is an idealized condition never achievable in practice.

In the evaluation above, we are considering ψ to be spatially uniform in the channel, a condition atypical for LCs, in which surface coupling and external fields generally produce distorted director patterns. In the N_F phase, spatial variations in **n** are controlled by nematic elasticity and by the coupling of **P** to electric fields—both external and internal—due to polarization space charge in bulk and on surfaces. The ratio $\sqrt{\epsilon K}/P$, where K is a Frank elastic constant ($K \approx 10^{-12}$ N), is very small (less than 1 nm), indicating that on all the length scales relevant here, electrostatics is dominant—a condition that makes the orientation response to external torques a spatially uniform ψ field[20].

In the channel experiments reported here, an external torque is produced by an applied electric field $\mathbf{E}_0$, forming an angle β with the channel axis (Fig. 2c). In this case, the torque balance condition is $\mathbf{P} \times \mathbf{E}_{int} = 0$, where $\mathbf{E}_{int} = \mathbf{E}_0 + \mathbf{E}_{depol}$ is the total electric field within the channel. For an applied field perpendicular to the channel axis ($\beta = 90°$), the depolarization field $\mathbf{E}_{depol}(\psi)$ arising from polarization charges on the channel walls cancels $\mathbf{E}_0$ for $E_0 < E_{sat}$, giving $\mathbf{E}_{int} = 0$ (refs. 21–23). Given the experimental applied fields ($E_0 \approx 1$ V mm^{-1}) and P_0, this cancellation occurs for sub-microradian reorientations of **P**, $\psi \approx E_0/E_{sat} < 10^{-7}$, leaving **P** always essentially parallel to the local channel axis.

The situation for an oblique applied field ($\beta < 90°$) is more subtle, as continuity of the parallel component of **E** across the channel boundary implies that $\mathbf{E}_{int} \neq 0$. In this case, the torque balance condition ($\mathbf{P} \times \mathbf{E}_{int} = 0$) is equivalent to the condition $\mathbf{P} \| \mathbf{E}_{int}$, which means that the perpendicular component of $\mathbf{E}_{int}$ is extremely small but non-zero. Here the continuity of $E_\parallel$ and $D_\perp$ (the normal component of the electric displacement) gives $\psi \approx (E_0/E_{sat})\sin\beta$. For typical experimental conditions, we have $\psi < 10^{-7}$ as before, so the normal component of $\mathbf{E}_{int}$ ($E_{int\perp} \approx E_0 \psi \cos\beta$) is not completely cancelled as in the perpendicular case but is made negligible via reduction by a factor of ~10^7.

Such immediate and effective screening, by which the normal component of E_0 is readily cancelled or made negligible by minuscule angular rotations, is a distinctive property of the N_F phase that we call fluid superscreening to mark the difference between this ultimately collective fluid dipolar reorientation and conventional dielectric or conductive screening by induced dipoles or free charges. By the way of coherent **P** tilting, fluid superscreening locally cancels the electric-field components normal to the channel walls but also globally affects its

longitudinal components through the long-range effect of the modified distribution of bound charges.

Ferroelectric superscreening intimately depends on the fluidity and orientational freedom of **P** and is thus specific to the N_F LC phase. In solid ferroelectrics, **P** derives from lattice deformations and can be inverted (but typically not reoriented) only when external fields overcome the coercive-field threshold. In these materials, polarization charges can be deposited only on specific crystal faces, giving rise to a depolarization field. In the absence of free charges on electrodes that compensate the surface polarization charges, the depolarization field opposes **P**, and the system reaches an equilibrium state controlled by the ratio between depolarization and coercive fields. In N_F materials, the orientational freedom of **P** implies the absence of a bulk coercive-field threshold, thus enabling fluid superscreening.

Ferroelectric nematics also bear important analogies to soft magnetic systems, that is, ferromagnetic solids with a particularly low coercive field, typically used in generators, transformers and switching circuits. Indeed, these materials are known to guide the magnetic field by cancelling its components normal to surfaces when larger than the coercive field. This phenomenon is normally understood in terms of mismatch between the large magnetic permeability of ferromagnets (up to $\mu_r \approx 10^5$ in mu-metals), and the small magnetic permeability of the surrounding non-magnetic materials. The analogy between these physically distinct systems makes the easy optical access to polar switching in N_F materials of potential interest for the understanding of soft ferromagnets and high-permittivity dielectrics.

Field-reversal experiments

To further explore the role of bound charge screening in the polarization following phenomenon, we investigated the response to the reversal of the sign of ΔV. On switching ΔV, the nematic order suddenly becomes unstable, with the transmitted light intensity through crossed polarizers (I_P) and without analyser (I_S) transiently changing during a time interval that depends on ΔV, being of the order of 100 ms for $E_0 = 1\,\mathrm{V\,mm^{-1}}$. Specifically, we have measured I_P versus time after field reversal in portions of the channels oriented parallel to the polarizer and thus dark in equilibrium before field reversal (Fig. 1c, bottom right). We normalized I_P by $I_{P_{45}}$, the value of I_P measured with the channel oriented at 45° with respect to the polarizer under equilibrium conditions before field reversal (Fig. 1c, top right). Similarly, we normalized I_S by I_{S_0}, the transmitted intensity under equilibrium conditions before field reversal. By inspecting the two transmittances $\tau_P(t) = I_P(t)/I_{P_{45}}$ and $\tau_S(t) = I_S(t)/I_{S_0}$, averaged over channel sections as a function of time together with the associated videos, we can identify three phases of polar switching in the channels: a disordering regime, a reorganization regime and a defect-annealing regime. Because of the small cross section of the microchannels, we could not experimentally measure the polarization current flowing through the electrodes to compare it with $\tau_P(t)$ and $\tau_S(t)$. We instead performed an analogous measurement on a flat cell that exhibits similar behaviour and an analogous $\tau_P(t)$ evolution (Supplementary Fig. 3).

The inspection of PTOM images and videos shows that on potential inversion (at $t = 0$), uniform polar order gives way to an irregular pattern composed of micrometre-sized domains (Fig. 3a,b) coherent with the notion that **P** locally rotates away from its original orientation in a variety of directions. This leads to an increase in $\tau_P(t)$ due to the optic axis rotation (Fig. 3d–g) and in a decrease in $\tau_S(t)$ due to scattering (Supplementary Fig. 4). The disorder in the N_F structure grows to a maximum and decreases, as shown by appearance of a minimum in $\tau_S(t)$ (that is, a maximum in turbidity) found at about the same time $t \approx t_m$ at which $\tau_P(t)$ shows a small minimum in its growth.

We find that t_m marks the transition between two different regimes. Pulsed field reversals, in which the sign of ΔV is inverted for a time $t_{inv} < t_m$, give rise to a simple exponential relaxation of $\tau_P(t)$, whereas for longer pulses (at $t_{inv} > t_m$), the relaxation process in the channel becomes much longer and irregular (Supplementary Fig. 5). We, thus, interpret t_m as the time it takes for the N_F domains to rotate enough to start reorganizing in the opposite direction via the coalescence of defect lines and interfaces that also reduces turbidity.

In the reorganization regime ($t > t_m$), $\tau_P(t)$ still grows, reflecting the coarsening and broadening of defects, to reach a maximum and decrease back to 0 when uniform polar ordering is established in the reversed direction. Such uniform N_F ordering develops through a nucleation process taking place in the narrowest section of the channel, typically (but not always) located halfway between the electrodes as a natural result of the etching process (Supplementary Section 1). This final stage in the reversal of **P** requires a major reorganization of the director field involving disentangling topological defects, closure of defect loops and reversal of surface polarity. Previous observations in silanized flat cells suggest the latter to be the slowest component of switching after field reversal[19].

After its nucleation, the defectless uniform region ($\tau_P = 0$) progressively expands via the motion of the interface separating the defected and defect-free N_F states (Fig. 3b (bottom) and Fig. 3c). Thus, the completion of **P** reversal takes place at a time that grows with the distance from the nucleation site, sooner in proximity of the channel centre (Fig. 3d, red line) and later (even after up to 1 s) close to the electrodes (Fig. 3d, blue and green lines).

New insights emerge from the comparison of $\tau_P(t)$ in distinct portions of the same channel and in different channels. First, the short-time behaviour is the same everywhere in all portions of the bent channels. This is shown in Fig. 3d for the S-shaped channel, whereas very similar results are obtained for the L- and Z-shaped channels. Second, $\tau_P(t)$ measured in the central portion of the bent channels, that is, close to the nucleation site, is nearly equal in all the regimes provided the applied voltage is the same (Fig. 3e shows data for $\Delta V = 0.5$ V). Remarkably, $\tau_P(t)$ is instead different for the simple straight geometry, which displays a slower rise and a steeper decay.

Figure 3f shows that polarization reversal is a process fully controlled by electrical interactions: the evolution of $\tau_P(t)$ becomes faster for larger ΔV (and hence E_0) with its whole kinetics being proportional to E_0 in all the regimes, as shown in the collapsed data (Fig. 3g). The small minimum at $\tau_P(t_m)$ is more pronounced for larger E_0, a condition in which we also find a larger turbidity (Supplementary Section 4). This behaviour reflects the fact that faster switching occurs through the breaking up of the system into smaller domains, leading to more scattering of light.

By demonstrating that the polarity inversion depends linearly on E_0, the results in Fig. 3f,g convey the notion that the shape of $\tau_P(t)$ can be used as an indirect readout of the local field E_L. Specifically, the identical growth of $\tau_P(t)$ for $t < t_m$ in the various portions of the S-shaped channel (Fig. 3d) indicates that in these regions, the average electric field is the same during this time interval and thus uniform throughout the channel. Analogous results have been found for the other bent channels. Moreover, the identical overall shape of $\tau_P(t)$ in the central part of the L-, Z- and S-shaped channels reveals that E_L is the same in the central portion of all the bent channels, provided that the width, ΔV and ℓ are the same.

In the latest stage of switching, defect-free N_F domains nucleate in the narrowest sections of the channels, suggesting that those are the places where E_L is the largest, and expand via a moving interface. We measured the propagation velocity v_I of such interfaces for varying ΔV values in a small region close to the nucleation spot. We find v_I to be constant, and thus well defined, at least for the first 100 µm of displacement, away from the electrodes and channel bends (Supplementary Fig. 6). In Fig. 3h, we plot v_I versus ΔV for the various channels. We find v_I to be approximately linear in ΔV and to be very similar in all the bent channels. Again, the straight channel is an exception, with a larger, nearly double, v_I.

https://doi.org/10.1038/s41567-023-02150-z

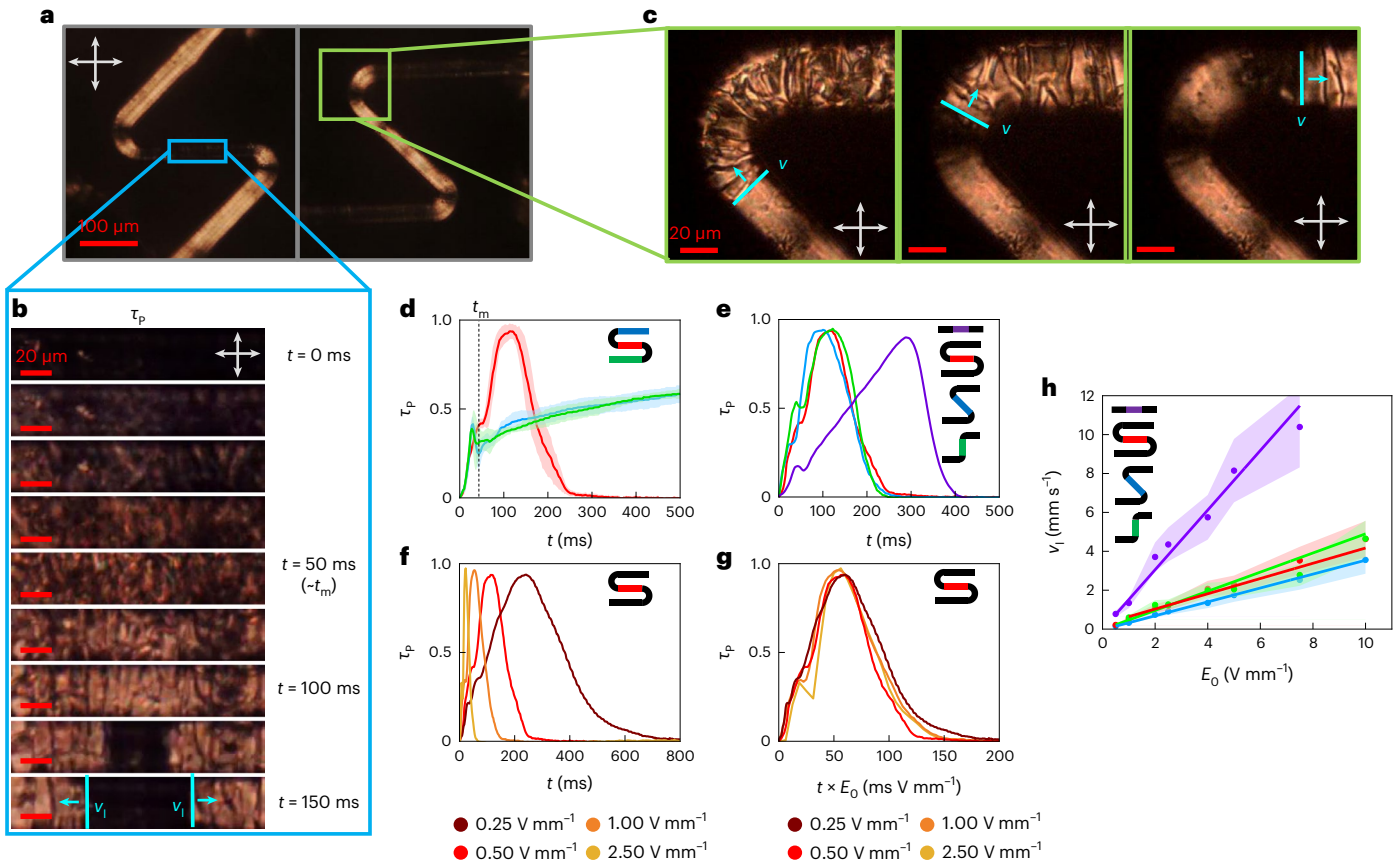

Fig. 3 | Polarization inversion in microchannels. a, PTOM image of the Z-shaped channel in two different orientations for $\Delta V = 1$ V. **b**, Time sequence of PTOM images of the central part of the Z-shaped channel following field inversion ($t = 0$). The sequence shows the appearance and coarsening of domains and the formation of the homogeneous-defected interface, which moves towards the electrodes with velocity v_I. **c**, Time sequence of PTOM images of a curve in the Z-shaped channel showing the motion of the homogeneous-defected interface with velocity v_I. **d**, Time evolution of the depolarized transmittance $\tau_P(t)$ measured in the central part and in the two side arms of an S-shaped channel during the inversion of ΔV from 0.5 to −0.5 V. Data are obtained as the average of six repetitions. The shadings illustrate standard deviations. **e**, Time evolution of the depolarized transmittance $\tau_P(t)$ measured in the central portion of the various types of channel during the inversion of ΔV from 0.5 to −0.5 V. Data are obtained as the average of six repetitions. Standard deviations, having values comparable with the ones in **d**, are omitted for clarity. **f**, Time evolution of the depolarized transmittance $\tau_P(t)$ measured in the central portion of an S-shaped channel during voltage inversion for varying ΔV values between the electrodes, corresponding to varying E_0 values, as shown in the legend. Data are obtained as the average of six repetitions. Standard deviations, having values comparable with the ones in **d**, are omitted for clarity. **g**, Data in **f** plotted as a function of the rescaled time tE_0. **h**, Velocity v_I of the homogeneous-defected interface versus nominal electric field E_0 measured in the central part of the various channels right after its formation. Data are presented as the average of four repetitions. The shadings illustrate the standard deviations, whereas the solid lines represent linear fits. All the experiments have been performed in the N_F phase at $T = 130$ °C.

The linear dependence of v_I on ΔV indicates that the motion of the interface is electrically driven and follows the local electric field, confirming that the latter is directed from electrode to electrode along the channels, despite their bends. Such motion also indicates that the interface carries electric charge. This is coherent with its marking a discontinuity in the polarization density between the fully polarized uniform phase and the less polarized defected structure, a concept that we further explored through the measurements of polarization current and transmittance in flat cells (Supplementary Fig. 3). The constant v_I for each ΔV reveals that the interface motion is opposed by a viscous-type friction force, probably somewhat reflecting the viscosity arising from director rotation within domains, necessary to free the volume from defects (Supplementary Section 7).

Continuum modelling of switching and equilibrium structure

To gain insights into the experimentally observed phenomena, we performed numerical simulations of the equilibrium structure and switching dynamics of N_F fluids confined to the microchannels. We assume that the ferroelectric polarization **P** has fixed magnitude P_0 but can vary in direction, that is, $\mathbf{P} = \mathbf{P}(\mathbf{r}) = P_0\mathbf{p}(\mathbf{r})$, where the polar director **p** is a unit vector, assumed to be parallel to the nematic director **n**. We further assume that the z dimension of the channels is large relative to the x and y dimensions, and that all quantities (**n**, **P**, **E**, ρ and so on) are independent of z, for example, $\mathbf{P}(\mathbf{r}) = \mathbf{P}(x, y)$. Finally, we assume that **P** and **E** are confined to the x–y plane, that is, $E_z = 0$ and $P_z = 0$. These simplifying assumptions result in a computationally tractable quasi-two-dimensional model that qualitatively captures the essential physics governing the behaviour of N_F fluids in microchannels. In fact, the polarization of an N_F LC confined to a channel with a z dimension much larger than its x and y dimensions will tend to orient along z in the absence of applied fields, so restricting **P** to the x–y plane is an artificial constraint that nevertheless enables us to explore the phenomena of superscreening and polarization following in the context of a minimal computational model.

The free-energy density of the ferroelectric nematic phase is taken to be the sum of the orientational elastic and electrostatic contributions, namely, $f(x, y) = f_{elast}(x, y) + f_{elect}(x, y)$. The former is the

Frank–Oseen orientational elastic free-energy density in the one-elastic-constant approximation, $f_{elast} = \frac{1}{2}K|\nabla\theta|^2$, where K is the elastic constant for splay and bend deformations and $\theta(x, y)$ is the orientation of $\mathbf{p}$ in the x–y plane. The electrostatic free-energy density is taken to be $f_{elect} = -\frac{1}{2}\mathbf{P}\cdot\mathbf{E}$, where $\mathbf{E}$ is the total electric field arising from both bound and free charges. There is an additional contribution to the electrostatic free energy in the presence of free charge (Supplementary Section 8), but this simple free-energy expression suffices to model the equilibrium structure and switching dynamics of N_F materials confined to channels. In our computational scheme, the bound charge distribution is calculated from $\rho_b = -\nabla\cdot\mathbf{P}$, and a smoothing procedure is employed so that both surface and volumetric bound charges can be treated on the same footing (Supplementary Section 8).

The equilibrium structure is obtained by the functional minimization of the total free energy, which we accomplish using a relaxation method: the system is evolved to obtain the equilibrium $\theta(x, y)$ by solving the equations of motion that result from setting the total torque (the sum of elastic, electrostatic and viscous torques) to zero.

The elastic, electric and viscous torques acting on $\theta(x, y)$ are $\tau_{elast}(x, y) = K\nabla^2\theta$, $\tau_{elect}(x,y) = \frac{1}{2}(\mathbf{P}\times\mathbf{E})\cdot\mathbf{z} = \frac{1}{2}P_0(E_y\cos\theta - E_x\sin\theta)$ and $\tau_{visc}(x, y) = -\gamma\partial\theta/\partial t$, where γ is the rotational viscosity. Starting from a given initial condition, the equations of motion are evolved to reach equilibrium ($\tau_{elastic} + \tau_{elect} = 0$), and the same equations of motion are solved to model the switching dynamics on field reversal. These equations are numerically solved, with θ defined on a discrete grid with grid spacing a, using an explicit Euler time-stepping scheme. The geometry of the simulated channels (S, L and I) matches that of the real channels in the x–y plane. For computational expediency, we perform simulations with a potential difference between the end of the channels of +1,000 V, that is, about 10^3 times larger than that applied in the experiments, since with this value, the entire switching process is largely complete within 500 µs. A grid spacing of $a = 1.5$ µm was used in the calculations presented here, but we have verified that varying grid spacings give similar results (Supplementary Section 8). In the simulations described below, we have also introduced homogeneous surface roughness of amplitude $\delta = 0.76$ µm into the channel boundaries, to more faithfully model the experimental situation (Supplementary Section 10 discusses the effects of surface roughness on the equilibrium structure and switching dynamics). Full details of the computational methods are also provided (Methods and Supplementary Sections 8–13).

Simulation results

The general features of the equilibrium structure and switching dynamics of ferroelectric nematics confined to microchannels can be understood from the simulated switching dynamics on voltage reversal for the S-shaped channel (Fig. 4). Figure 4a shows the time evolution of polarization density, total charge density and electric field on voltage reversal. Figure 4b,c shows the t dependence of $P_\parallel$ and $E_\parallel$, the components of $\mathbf{P}$ and $\mathbf{E}$ parallel to the local channel direction, respectively, averaged over the central linear section of the S-shaped channel, where the coloured vertical lines indicate the times corresponding to the snapshots (Fig. 4a) with matching coloured frames. Immediately after voltage reversal ($t = 0$), the electric field in the channel is non-uniform in magnitude and has a substantial component transverse to the channel. This transverse component of field is rapidly screened out by a slight reorientation of polarization at the channel surfaces, and by $t = 15$ µs (Fig. 4c, red vertical line), the electric field in the channel follows the channel contour and is nearly uniform in magnitude (~1 V µm^{-1}) (Fig. 4a, red frame). In this time interval, the field outside the channel switches direction, with a corresponding change in sign of the bound charge density at the channel surfaces. Figure 4d,e shows that the same field-reversal time interval during which $\mathbf{E}$ changes direction whereas $\mathbf{P}$ remains nearly constant is observed in different regions within the L-, S- and I-shaped channels, identified by the colour code in the schematic shown in Fig. 4d,e.

At the end of the field-reversal process, the polarization field in the channel is antiparallel to the electric field and thus in a state of unstable equilibrium, leading to the reorientation and disordering of the polarization field at later times. The configuration at time $t = 75$ µs (corresponding to $P_\parallel(t_2) \approx 0$) is shown in the blue-framed snapshots (Fig. 4a), where it appears that the inversion of $P_\parallel$ takes place through a disordered state, indicating that the reduction in free energy occurs via the breaking of the polar director field into small domains, enabling the local minimization of the energy cost of bulk and surface bound charge accumulation. The orientation of the electric field within the channel becomes somewhat disordered during this process, but overall $E_\parallel$ and ρ remain nearly constant in the interval $t = 25$–125 µs (Fig. 4b–e, blue shading)—the time interval during which $P_\parallel$ nearly completes its inversion. Thus, most of the $\mathbf{P}$ inversion process takes place while $E_\parallel$ is roughly constant and uniform. Very similar behaviour of $P_\parallel$ and $E_\parallel$ is found over this time interval for different regions of the various channels (Fig. 4d,e).

Polarization reversal is not the final event in the voltage-reversal response. Indeed, a complex subsequent dynamics takes place, involving a more subtle reorientation of the polarization field and an associated reorganization of the bound charge in bands of positive and negative signs transverse to the channel, resulting in non-uniformity in the magnitude of the electric field along the channel, evident by $t = 250$ µs (Fig. 4a, purple frame). In this last stage, $E_\parallel(t)$ evolves differently in different regions of the various channels (Fig. 4e, $t > 125$ µs) and sensitively depends on the details of channel roughness, as evident from the comparison with simulations involving channels in which the linear portions of the channels are smooth (Supplementary Section 10 provides the data and discussion).

Switching in the simulated microchannels, thus, takes place in three distinct stages: (1) superscreening of the normal component of the electric field at the boundaries of the channel leading to uniform following of the channel contour by the electric field, and accompanied by a reversal of the field direction outside the channel and an associated change in the sign of bound charge at the surface of the channel; (2) reversal of the polarization direction via a disordered intermediate state, culminating in uniform following of the channel contour by the polarization field, whereas $\mathbf{E}$ within the channel remains approximately uniform in magnitude and guided; (3) roughness-dependent reorganization ('annealing') of the polarization field and associated bound charges within the channel.

To clarify the role of channel width variation, we also performed simulations of S- and I-shaped channels tapered in the central region, finding that polarization reversal is faster and the local field is larger where the channel has the minimum width, consistent with experimental observations (Supplementary Section 11).

Finally, to elucidate the qualitative differences between high-polarization N_F materials and high-dielectric-constant materials, we have modelled linear, isotropic dielectrics with relative permittivity ϵ_r confined to channels under constant-voltage conditions identical to those applied to confined ferroelectric nematics (Supplementary Section 13). We find that the behaviour of channel-confined linear dielectrics with large relative permittivities ($\epsilon_r \geq 100$) bears a strong qualitative resemblance to that of channel-confined N_F materials, in that the electric field and polarization (here proportional to the electric field) follow the contour of the channel, with a small normal component of electric field at the internal boundaries of the channel, due to the large dielectric mismatch with the surrounding medium (assumed to have $\epsilon_r = 1$). The magnitude of the field in dielectric-filled channels is highly uniform in the high-ϵ_r limit, and is relatively insensitive to surface roughness compared with N_F LCs (Supplementary Fig. 35). As discussed in the Supplementary Information, these features reflect the absence of bound charge in the volume of dielectric-filled channels,

https://doi.org/10.1038/s41567-023-02150-z

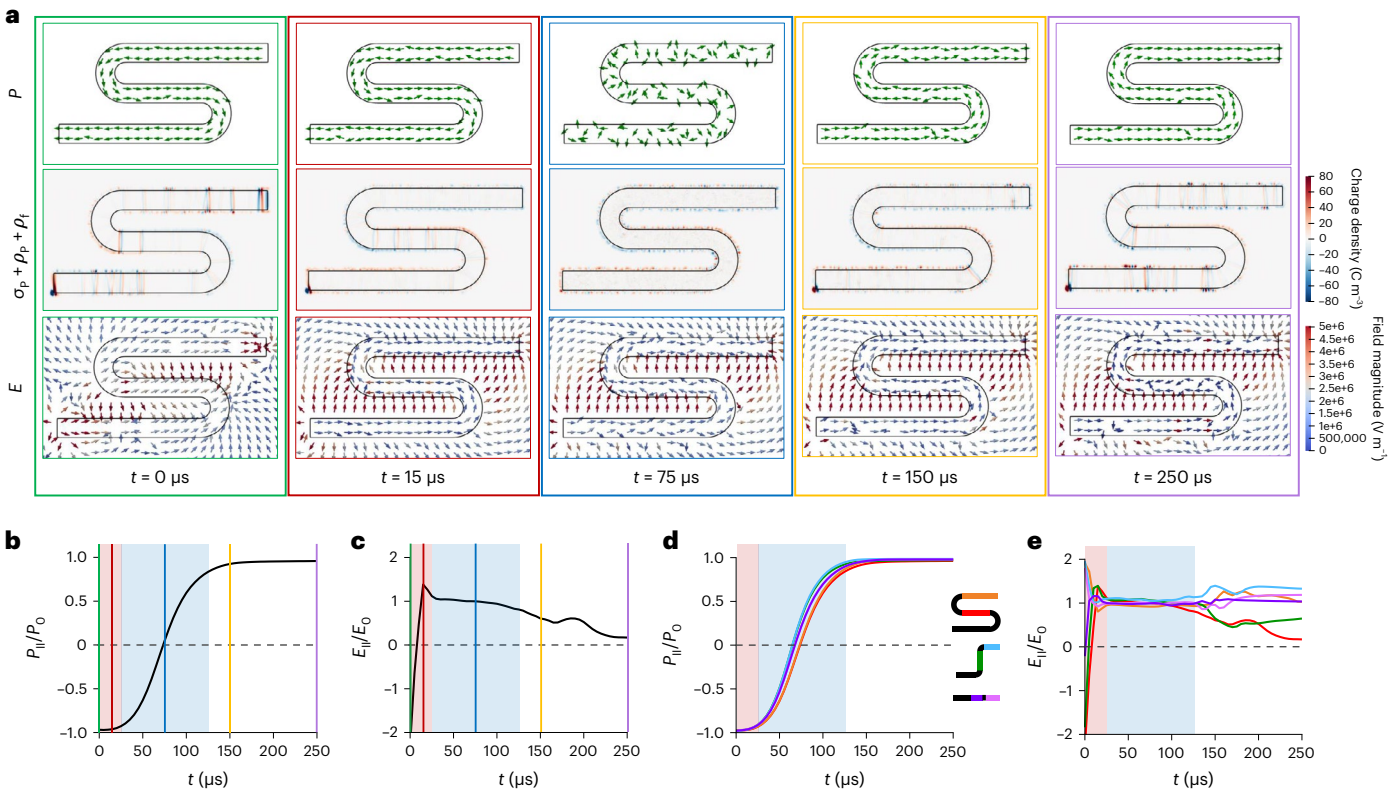

Fig. 4 | Simulated time evolution of polarization P, total (bound plus free) charge density $\rho = \sigma_P + \rho_P + \rho_f$ and electric field E, following sign reversal of the potential on the electrodes (at $t = 0 = t_0$). The starting condition is the equilibrium configuration for the opposite sign of potential difference. All the channels are of width 40 μm and contour length $\ell \approx 1$ mm. **a**, Snapshots showing **P**, ρ and **E** in the S-shaped channel at five specific times (marked by the colour frames). The arrows denoting **P** and **E** are of a fixed size, with the field amplitude indicated by the colour of the arrows. For clarity, **P** and **E** are shown only at a subset of grid points (1 in 196). **b**,**c**, $P_\parallel(t)$ (**b**) and $E_\parallel(t)$ (**c**) averaged over the central section of an S-shaped channel. The vertical coloured lines mark the times relative to the snapshots in **a** of a matching colour. **d**,**e**, $P_\parallel(t)$ (**d**) and $E_\parallel(t)$ (**e**) from different regions of the S-, L- and I-shaped channels, with the colour code indicated in the schematic. The colour shading in **b**–**e** highlights the time intervals during which the electric field reverses (red shading) and during which the polarization reverses and $E_\parallel \approx 1\,\mathrm{V\,\mu m^{-1}} \approx \Delta V/\ell$, indicating electric-field guiding (blue shading).

a consequence of their linear field response. Owing to their large spontaneous polarization, N_F materials have a highly nonlinear response to applied fields and support volumetric bound charge distributions arising from the divergence of the polarization field, giving rise to complex physical phenomena that are qualitatively distinct from those of linear dielectrics.

Discussion

Despite the strong simplifications adopted in the model, the simulation results clearly confirm that the major experimental observations are a direct consequence of the unique features of the fluid N_F state. The polarization continuously follows the channels from electrode to electrode even in bent-shaped geometries, in full agreement with the experimental observations. The simulations confirm the essential role of N_F superscreening, through the prompt accumulation of surface polarization charges that screen the component of **E** normal to the channel boundaries, causing the electric field inside each channel to become directed along the channel, with a magnitude that—during switching—is roughly constant and uniform in all the channels. This is consistent with the experimental observation that the initial stages of switching kinetics are similar in different regions of the bent channels. Simulations also qualitatively confirm that the observed disruption of nematic ordering through the formation of small domains in the initial stages of **P** switching is a consequence of bulk polarization, a strategy by which the system minimizes the bulk and surface bound charge during inversion.

On longer timescales, simulation predicts variations in the electric-field magnitude that depend on the detailed shape of the channel. Experiments indicate that in the latest stages of **P** inversion, the defect-free volume nucleates in the narrowest sections of the channels where simulation suggests the field is the largest, a finding reminiscent of the magnetic-field behaviour in electromagnets, where the field magnitude in the air gap can be increased with a conical ferromagnetic core. The expansion velocity of such domains (v_l) is equal in the bent channels, indicating that the magnitude of the electric field is equal in the central part of the S-, Z- and L-shaped channels. To assess the quantitative coherence of these observations, a much more detailed level of modelling is required.

Experiments show that straight channels behave a bit differently than bent ones, with a slower onset of **P** disordering and a larger v_l. This is not in simple agreement with simulations, which predict similar dynamics for all the channel geometries with rough boundaries. Even in simulation, however, the straight channel has a singular behaviour: straight channels with smooth walls show a much slower **P** inversion, and tapering and/or introducing wall roughness has a much more dramatic effect than in bent channels (Supplementary Section 11). We understand the slow response of the smooth straight channel to be a consequence of its symmetry, with no points of bound charge accumulation available to 'nucleate' polarization reversal, as in the bends of the other channels. The elimination of the normal component of **E** in the straight channel requires the buildup of a non-zero $\nabla \cdot \mathbf{P}$, whereas bending, tapering and wall noise provide immediate accumulation

points for polarization charges, speeding up the charge distribution process. We, thus, speculate that the quantitative features of switching in the straight channel sensitively depend on its construction details.

Conclusions

The electric-field response of ferroelectric nematics confined to bent microchannels, in which polarization and electric field follow the channels along their paths, brings to light the capacity of these materials to promptly cancel any electric-field component normal to the dielectric surfaces. This unique and defining property of N_F materials, which we call fluid superscreening, is achieved through minor local changes in the orientation of **P** and is the leading and fastest component of the multiscale dynamic response of N_F to electric fields, determining all the subsequent time evolution.

Superscreening mandates that the electric field within the channel 'follows' the contour of the channel, which further implies that the ferroelectric polarization field is guided by the channel under equilibrium conditions because the electrostatic energy is minimized when the polarization field is locally parallel to the electric field everywhere. This behaviour strictly depends on the electrostatic energy being the dominant free-energy contribution (under our conditions about 10^4 times larger than the elastic energy (Supplementary Section 12))—a feature that makes ferroelectric nematics strikingly different from conventional non-polar nematics.

The S-shaped channel, in which there are three parallel linear sections, is particularly revealing: in principle, the polarization field could point in the same direction (say, to the right) in all the three sections, with polarization reversal walls in the two curved portions of the channel. However, such polarization reversal walls are highly charged and thus inherently unstable, with their bound surface charge density of almost $\pm 2P_0$ giving rise to fields on the order of 10^7 V mm^{-1}. Should such reversal walls transiently form, the large electric field they generate would immediately reorient the polarization in the central portion of the S-shaped channel to produce uniform 'polarization following' along the channel contour, as observed.

Superscreening operates at the N_F–dielectric interface, but not when the N_F material is in direct, high-capacitance contact with the electrodes, such as those at the ends of the channels in the experiments described here, where bound polarization charges are effectively compensated by free charges—a condition enabling the strong electro-optical response observed following potential reversal.

The last step in the switching involves the annealing of defects in the bulk and polarity inversion at the surfaces. This occurs through a nucleation process that starts where the field is the largest and propagates through the entire channel via an electrophoretic-type motion of the interface between uniform and disordered regions. We find the whole behaviour to be electrically driven and thus specific to this fluid ferroelectric phase in which electrostatic interactions dominate.

Our findings raise the possibility of exploiting the propagation of order within channels to design microconfinement geometries that provide a simple means to control the optical axis in multiple positions in electro-optic devices. More broadly, this study establishes a conceptual framework for understanding the behaviour of N_F materials in a variety of settings in which geometrical confinement effects are relevant, for example, in composite structures, in porous and/or disordered media with quenched or annealed disorder and in the presence of topographically patterned substrates.

Online content

Any methods, additional references, Nature Portfolio reporting summaries, source data, extended data, supplementary information, acknowledgements, peer review information; details of author contributions and competing interests; and statements of data and code availability are available at https://doi.org/10.1038/s41567-023-02150-z.

References

1. Weiss, P. L'hypothèse du champ moléculaire et la propriété ferromagnétique. *J. Phys. Theor. Appl.* **6**, 661–690 (1907).
2. Debye, P. Einige resultate einer kinetischen theorie der isolatoren. *Phys. Z.* **13**, 97–100 (1912).
3. Born, M. Über anisotrope flüssigkeiten. Versuch einer theorie der flüssigen kristalle und des elektrischen kerr-effekts in flüssigkeitenn. *Sitzungsber. Preuss. Akad Wiss.* **30**, 614–650 (1916).
4. Mandle, R. J., Cowling, S. J. & Goodby, J. W. A nematic to nematic transformation exhibited by a rod-like liquid crystal. *Phys. Chem. Chem. Phys.* **19**, 11429–11435 (2017).
5. Nishikawa, H. et al. A fluid liquid-crystal material with highly polar order. *Adv. Mater.* **29**, 1702354 (2017).
6. Chen, X. et al. First-principles experimental demonstration of ferroelectricity in a thermotropic nematic liquid crystal: polar domains and striking electro-optics. *Proc. Natl Acad. Sci. USA* **117**, 14021–14031 (2020).
7. Lavrentovich, O. Ferroelectric nematic liquid crystal, a century in waiting. *Proc. Natl Acad. Sci. USA* **117**, 14629–14631 (2020).
8. Mertelj, A. et al. Splay nematic phase. *Phys. Rev. X* **8**, 041025 (2018).
9. Chen, X. et al. Polar in-plane surface orientation of a ferroelectric nematic liquid crystal: polar monodomains and twisted state electro-optics. *Proc. Natl Acad. Sci. USA* **118**, e2104092118 (2021).
10. Sebastián, N., Mandle, R. J., Petelin, A., Eremin, A. & Mertelj, A. Electrooptics of mm-scale polar domains in the ferroelectric nematic phase. *Liq. Cryst.* **48**, 2055–2071 (2021).
11. Feng, C. et al. Electrically tunable reflection color of chiral ferroelectric nematic liquid crystals. *Adv. Opt. Mater.* **9**, 2101230 (2021).
12. Barboza, R. et al. Explosive electrostatic instability of ferroelectric liquid droplets on ferroelectric solid surfaces. *Proc. Natl Acad. Sci. USA* **119**, e2207858119 (2022).
13. Sebastián, N., Čopič, M. & Mertelj, A. Ferroelectric nematic liquid-crystalline phases. *Phys. Rev. E* **106**, 14629–14631 (2022).
14. Marni, S., Nava, G., Barboza, R., Bellini, T. G. & Lucchetti, L. Walking ferroelectric liquid droplets with light. *Adv. Mater.* **35**, 2212067 (2023).
15. Mandle, R. J., Cowling, S. J. & Goodby, J. W. Rational design of rod-like liquid crystals exhibiting two nematic phases. *Chem. Eur. J.* **23**, 14554–14562 (2017).
16. Li, J. et al. Development of ferroelectric nematic fluids with giant-ϵ dielectricity and nonlinear optical properties. *Sci. Adv.* **7**, 5047–5068 (2021).
17. Marcinkevičius, A. et al. Femtosecond laser-assisted three-dimensional microfabrication in silica. *Opt. Lett.* **26**, 277–279 (2001).
18. Osellame, R., Hoekstra, H. J., Cerullo, G. & Pollnau, M. Femtosecond laser microstructuring: an enabling tool for optofluidic lab-on-chips. *Laser Photonics Rev.* **5**, 442–463 (2011).
19. Caimi, F. et al. Surface alignment of ferroelectric nematic liquid crystals. *Soft Matter* **17**, 8130–8139 (2021).
20. Zhuang, Z., Maclennan, J. E. & Clark, N. A. Device applications of ferroelectric liquid crystals: importance of polarization charge interactions. *Proc. SPIE* **29**, 110–114 (1989).
21. Clark, N. A., Coleman, D. & Maclennan, J. E. Electrostatics and the electro-optic behaviour of chiral smectics C: 'block' polarization screening of applied voltage and 'V-shaped' switching. *Liq. Cryst.* **27**, 985–990 (2000).
22. Shen, Y. et al. Effective conductivity due to continuous polarization reorientation in fluid ferroelectrics. *Phys. Rev. E* **84**, 020701 (2011).
23. Coleman, D. et al. Control of molecular orientation in electrostatically stabilized ferroelectric liquid crystals. *Phys. Rev. Lett.* **91**, 175505 (2003).

Methods

Materials

RM734 (4-[(4-nitrophenoxy)carbonyl]phenyl 2,4-dimethoxybenzoate) has been synthesized as reported elsewhere[6]; all the other reagents and materials were obtained from different commercial sources.

Channel fabrication

Microchannels have been fabricated by femtosecond laser irradiation followed by chemical etching[17,18] in 1-mm-thick fused silica substrates. Supplementary Section 1 provides details of the whole process. Following laser irradiation, we have exposed the substrate to two different etchant solutions: first, an aqueous solution of hydrofluoric acid to etch the access holes, and then a solution of potassium hydroxide to etch the channels. We have used this dual process to benefit from the advantages of both etchants. Indeed, hydrofluoric acid guarantees a high etching rate for large volume removal, that is, for the creation of electrode access holes, whereas potassium hydroxide is slow but provides high etching selectivity for controlled and uniform microchannel cross section over the entire length[24]. To smooth the microchannel surfaces, we annealed the samples in a temperature-controlled furnace[25]. Channel surfaces have then been treated using a modified version of the procedure reported in another work[19].

Transmittance measurements

Transmitted light intensities through crossed polarizers (I_P, $I_{P_{45}}$) and without an analyser (I_S, $I_{P_{45}}$) are measured by recording 400 fps videos with a complementary metal–oxide–semiconductor microscope camera. The analyses are performed on a $30 \times 30\ \mu m^2$ region, aligned along the polarizers (and thus dark in stationary conditions) and centred on the interface nucleation point for measurements in the central branches and at halfway in the lateral branches. The intensity of the first frame has been subtracted as a background. Transmittance through crossed polarizers $\tau_P(t)$ is calculated as the ratio between $I_P(t)$ and the intensity measured in stationary condition at 45° with the polarizer. Transmittance without the analyser $\tau_S(t)$ is calculated as the ratio between $I_S(t)$ and the intensity measured under the stationary condition at the instant t_0 (I_{S_0}). All the measurements are obtained as an average of at least three negative-to-positive voltage switches and three positive-to-negative voltage switches.

Measurements of v_I

To perform v_I measurements, 500 fps videos are recorded with a complementary metal–oxide–semiconductor microscope camera and analysed with an edge-tracking MATLAB R2021a script (Supplementary Section 6 provides more details). Measurements are referred to a single interface and recorded in the first instants after its formation. All the measurements are obtained as an average of at least two negative-to-positive voltage switches and two positive-to-negative voltage switches. Error shading represents the standard deviation.

Simulations

The dynamical evolution and equilibrium structure observed in our simulations depend on the initial conditions and other details of the simulations, and we have carried out a variety of numerical experiments to assess these dependencies. For the results presented here, we adopt the following simulation protocol, designed to minimize the dependence on initial conditions: (1) initialize the system with a completely random polar director field (the polar angle θ at each grid point is assigned a random value in the range $-\pi$, π); (2) evolve the system forward in time for 510 μs and maintain a constant potential difference of −1,000 V between the two ends of the channel; (3) change the sign of the voltage between the ends of the channel to +1,000 V and evolve the system forward in time for 500 μs. Here we present results from stage (3) of these simulations, under the assumption that this models the experimental switching dynamics at a qualitative level, and that the final configuration is a reasonable model of the equilibrium state of the system for a fixed applied voltage. In our model, the free charge on the electrodes is represented by a uniform charge density located at and spanning the channel ends, with equal and opposite magnitude at the two ends of the channel. A constant electrostatic potential difference ΔV between the two ends of the channel is maintained by appropriately scaling the free-charge density at each timestep. Supplementary Sections 8–13 provide full details of the theoretical model and computational methods.

Data availability

Source data are provided with this paper.

Code availability

The custom code used to generate the results reported in this manuscript is available from M.A.G. upon request.

References

24. LoTurco, S., Osellame, R., Ramponi, R. & Vishnubhatla, K. C. Hybrid chemical etching of femtosecond laser irradiated structures for engineered microfluidic devices. *J. Micromech. Microeng.* **23**, 085002 (2013).
25. Sala, F., Paié, P., Martínez Vázquez, R., Osellame, R. & Bragheri, F. Effects of thermal annealing on femtosecond laser micromachined glass surfaces. *Micromachines* **12**, 180 (2021).

Acknowledgements

F.C., G.N., S.F. and T.B. acknowledge support from MIUR-PRIN (2017Z55KCW). X.C., N.A.C. and M.A.G. acknowledge support for publication of this work from NSF Condensed Matter Physics grants (DMR 1710711 and DMR 2005170).

Author contributions

F.C., L.L., M.A.G. and T.B. conceived the experiment. F.C., G.N., R.O. and T.B. designed the experiment. F.C., S.F., P.P. and X.C. performed the experiment. M.A.G. designed and performed the simulation. F.C., S.F., G.N., M.A.G. and T.B. analysed the data. F.C., N.A.C., M.A.G. and T.B. interpreted the results. F.C., L.L., P.P., N.A.C., M.A.G. and T.B. wrote the paper.

Competing interests

The authors declare no competing interests.

Additional information

Supplementary information The online version contains supplementary material available at https://doi.org/10.1038/s41567-023-02150-z.

Correspondence and requests for materials should be addressed to Matthew A. Glaser or Tommaso Bellini.

Peer review information *Nature Physics* thanks Alenka Mertelj and Satoshi Aya for their contribution to the peer review of this work.